Exfoliated nanoplatelets of an Aurivillius phase, $Bi_{3.25}La_{0.75}Ti_3O_{12}$: Characterisation by X-ray diffraction and by high-resolution electron microscopy

Virginie Chevallier*, Geneviève Nihoul, Véronique Madigou

Laboratoire Matériaux et Microélectronique de Provence, CNRS UMR 6137, Université du Sud Toulon Var, BP 20132, 83957 La Garde Cedex, France

Abstract

Nanoparticles of the Aurivillius phase La-substituted BTO ($Bi_{4-x}La_xTi_3O_{12}$, with $x = 0.75$) were obtained through a chemical lithiation process. They have been characterised by X-ray diffraction and transmission electron microscopy (diffraction and imaging at high resolution). The defect-free particles are platelet-shaped with the c large axis perpendicular to the plane. From high-resolution images, it is clear that the delamination process occurs at the level of the $(Bi_2O_2)^{2+}$ intermediate layer and is destructive for this layer. The smallest thickness measured corresponds to one cell parameter (3.3 nm) but a large range of thicknesses have been observed: this suggests that the lithium insertion does not take place in all $(Bi_2O_2)^{2+}$ layers, despite a large excess of lithium and a long reaction time. This is confirmed by ICP analysis, which leads to a formula $Li_{0.99}Bi_{3.25}La_{0.77}Ti_{3.00}O_{12}$ for the lithiated compound. This behaviour towards lithium intercalation differs from those observed with BTO in literature, where lithium insertion is reported as occurring in every $(Bi_2O_2)^{2+}$ layer. Possible explanations for this difference are advanced based on microstructural and structural considerations.
© 2008 Elsevier Inc. All rights reserved.

Keywords: Aurivillius phases; $Bi_{3.25}La_{0.75}Ti_3O_{12}$; Layered perovskites; Lithium intercalation; *n*-Butyllithium; Exfoliation

1. Introduction

In recent years, the principles of soft chemistry have been extensively used to design new "layered perovskites" materials, starting from a variety of compounds such as Dion–Jacobson [1,2] (D–J), Ruddlesden–Popper [3–5] (R–P) and Aurivillius [6,7] phases. The common feature of these materials is that they themselves are layered perovskites, that is to say, intergrowths of perovskite and intermediate layers. For D–J and R–P phases, these intermediate layers are cations while for Aurivillius phases they consist in a covalent network of $(Bi_2O_2)^{2+}$. Known since the early 1970s [8–10] for its promising ferroelectric properties, $Bi_4Ti_3O_{12}$ (or rather $Bi_2O_2[Bi_2Ti_3O_{10}]$) is a famous member of this latter family. Schaak and Mallouk [11] presented a powerful toolbox of solid-state reactions

for retrosynthetically synthesising new perovskites. As an extension of the toolbox, the authors proposed to exploit the exfoliation and the layer-by-layer restacking of layered perovskites as thin films, in order to synthesise new perovskites with complex stacking sequences. If smectite clays such as montmorillonite spontaneously exfoliate in water [12], modifications of the interlayer surfaces are often necessary to lower layer charge in order to promote exfoliation [13]. Thus, exfoliation was readily achieved for the proton forms of D–J [14,15] and R–P [16,17] phases, upon reaction with a bulky organic base. Recently, Kim et al. [18] have synthesised $Li_2Bi_4Ti_3O_{12}$ (Li-BTO) by the reaction of the Aurivillius phase $Bi_4Ti_3O_{12}$ (BTO) with *n*-butyllithium (*n*-BuLi), and exfoliated it in water. The authors also characterised the stable lithiated compound, Li-BTO, by neutron diffraction and X-ray absorption spectroscopy, isolated before exfoliation in water [19]. However, the interest for BTO has slowed down as investigations have revealed that BTO ferroelectric films suffer from fatigue [20] and exhibit much lower values of

*Corresponding author. Fax: +33 494 142 168.

E-mail addresses: chevallier@univ-tln.fr (V. Chevallier),
nihoul@univ-tln.fr (G. Nihoul), madigou@univ-tln.fr (V. Madigou).

switching polarisation than the bulk material, impeding using it for integration in FeRAMs. It has also been shown that partial substitution of Bi^{3+} cations by La^{3+} cations improves the properties of thin films for memory applications [21–25]. Hence, as the La-substituted BTO (BLT) internal structure is different from the BTO one, it was interesting to study if BLT powders could be exfoliated as BTO compounds. Here we report X-ray diffraction (XRD) and transmission electron microscopy (TEM) studies on lithiated-BLT and exfoliated BLT nanosheets (exf-BLT). In addition to what was done on BTO [18], a fine analysis of the atom stacking in the individual BLT nanosheets of the exfoliated product has been made by high-resolution transmission electron microscopy (HREM) as detailed characterisation is necessary to reveal stacking faults that are expected in these materials [11]. The BLT pristine material has also been characterised in order to compare structural and morphological features at different stages of the synthesis.

2. Experimental

2.1. BLT powder synthesis

$Bi_{3.25}La_{0.75}Ti_3O_{12}$ (BLT) polycrystalline samples were prepared by conventional solid-state reaction. Bi_2O_3 (Aldrich; 99.9%), La_2O_3 (Acros; 99.99%) and TiO_2 (Aldrich; 99 + %) were used as starting materials. La_2O_3 was first pre-calcined at 850 °C overnight in order to remove carbonates and hydroxides. The three oxides were mixed in stoichiometric amounts, thoroughly ground, pressed into pellets, calcined at 700 °C for 12 h in air (heating rate 5 °C/min) and then slowly cooled to room temperature. The pellets were then ground again and the eventual presence of other phases was checked by XRD. The heat treatment was repeated once at 900 °C then at 1050 °C, until no other phases than BLT were detected and no more changes in the lattice parameters could be observed. Before and after each heat treatment, the pellets were weighted to verify that no bismuth had been lost. At the end of these treatments, a white powder of BLT was obtained.

2.2. Chemical lithium intercalation

Reductive lithium intercalation was carried out by reacting the ground BLT sample with 3 mol-excess *n*-BuLi (1.6 M in hexane; Acros) in N_2 atmosphere at room temperature for 3 days, under stirring, according to the same protocol as described by Kim et al. [18]. The lithiated BLT was then obtained as a black powder, which had to be thoroughly washed with hexane in order to remove unreacted *n*-BuLi. The powder was completely black which proves that all the BLT grains have been modified. The atomic composition of the lithiated sample was determined by ion-coupled plasma (ICP) analysis.

2.3. Chemical lithium de-intercalation and exfoliation

Oxidative lithium de-intercalation was produced by setting the Li-BLT black powder in ultra-pure deionised water (DI water) under ultrasonic radiation, during at least 2 days. This procedure leads to the exfoliation of the layered material, which can be followed by the gradual change in colour of the powder, from black to white. Thus, BLT nanosheets were obtained as an aqueous colloidal suspension which was centrifuged (6000 rpm, 1 h) to collect the nanosheets as an aggregate in the bottom of the tube. In order to remove LiOH, this glue-like solution was then washed several times with DI water until the pH of the supernatant became 7. The nanosheets were then redispersed in DI water under ultrasonic radiation. The obtained suspension was again centrifuged (6000 rpm, 1 h) in order to separate the bigger particles from the smaller ones: the centrifugation speed was chosen not too high to expel only the large particles. At this stage, the supernatant was clear and colourless.

2.4. X-ray diffraction

Crystalline phase identification and lattice parameters were obtained from powder XRD with a Siemens D-5000 diffractometer in reflection mode, using $CuK\alpha$ radiation and equipped with a diffracted-beam monochromator and Soller slits. Unless otherwise specified, data were collected at room temperature in the angular range 10–86° in 2θ with steps of 0.02°. Data analysis was carried out by profile matching method using the FULLPROF program suite [26]. For instrumental profile calibration, a sample of yttrium iron garnet (YIG) was used. For characterisation on the nanosheets, droplets were removed in the clear supernatant, deposited on a Si substrate and evaporated at ambient temperature.

2.5. Transmission electron microscopy (TEM)

TEM images, both in low magnification and in high resolution (HREM), were obtained with a Tecnaï G^2 microscope, working at a voltage of 200 kV (associated wavelength 2.51 pm) with a point-to-point resolution of 0.24 nm. The pristine and the lithiated powders were crushed in ethanol and then a drop of the dispersion was put on a holey carbon grid. For the exfoliated powder, the sample was prepared by dripping drops of the clear supernatant onto the holey carbon grid. Local chemical analyses were performed using the energy dispersive X-ray spectroscopy (EDS) system attached to the microscope. Image simulations were performed using the JEMS program [27] based on the multislices method.

3. Crystallography

BTO can be described as a piling up of three pseudo-perovskite groups with Ti^{4+} cations inside the octahedra

and Bi^{3+} ions in the A position ($A_{n-1}B_nO_{3n+1}$ with $n = 3$). Between these pseudo-perovskite groups, there is a layer with an oxygen plane between two Bi^{3+} cations planes (Bi_2O_2). This structure corresponds to a slight deformation of a tetragonal structure with the space group $I4/mmm$. It has been shown that the space group is $B1a1$ which corresponds to a monoclinic symmetry [28]. In fact, the monoclinic structure is a distortion of an orthorhombic structure described in the $B2cb$ space group. The deviation between the two systems is very small and for most cases it is very difficult to experimentally differentiate them. So, in agreement with Hervoches and Lightfoot [29], in this study we have chosen to use the $B2cb$ space group. In the $Bi_{4-x}La_xTi_3O_{12}$ phase, the La^{3+} substitution for Bi^{3+} leads to a light variation of the parameters compared with BTO. In the $B2cb$ space group, c is the large axis ($c = 3.290$ nm), a is the two-fold axis ($a = 0.5423$ nm) and the b parameter is equal to 0.5419 nm. The position of the La^{3+} cations is still discussed; for some authors La^{3+} cations substitute for Bi^{3+} cations in the perovskite units only [30,31] and for others there is a cationic disorder between the two different sites of Bi^{3+} cations [32,33]. The cation disorder increases with the substitution ratio and seems to depend on the annealing temperature. For $x = 0.75$, the La^{3+} cations are usually said to be mainly in the A position [30,31,34]. An important point to note is that there are 14 cations planes and 16 oxygen atoms planes stacked along the c-axis and that the spacing between the former varies from 0.204 to 0.268 nm. Finally, one can notice that a cell comprises two identical groups consisting of three pseudo-perovskite blocks and one intermediate layer along the c-axis, translated by $(a+c)/2$.

Li-BTO has been studied by Choy et al. [19]; they give a structure with the same space group than BTO where the Li^+ ions are in the cations planes of the $(Bi_2O_2)^{2+}$ layer. The parameters are only slightly different from BTO (variation of 3.10^{-4} nm for a, 1.10^{-4} nm for b and 15.10^{-4} nm for c).

BTO and Li-BTO structures (from data of Hervoches and Lightfoot [29] and Choy et al. [19], respectively) are shown in Fig. 1 where the projections along the [110] axis are drawn; this direction of projection and the [100] one are mainly used in high-resolution electron microscopy (HREM). Along the [110] axis, the bismuth ions in the intermediate layer show a zigzag pattern and one can see the translation of the perovskite group at the intermediate layer level, while these features are not visible along the a-axis.

4. Results

4.1. XRD analyses

The patterns collected on the BLT pristine material, the lithiated compound (Li-BLT) and the exfoliated material are presented in Fig. 2. Despite very long step counting times (50 s both for BLT and Li-BLT and 200 s for
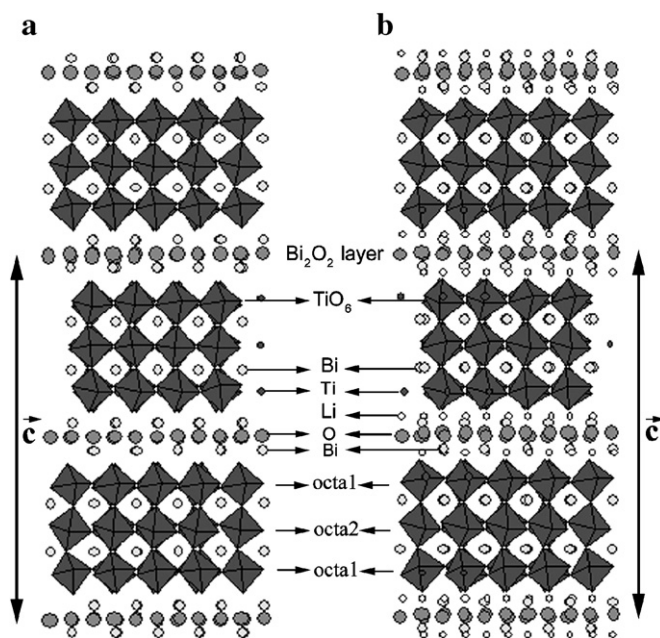

Fig. 1. (a) Projection of $Bi_4Ti_3O_{12}$ cell along [110]. (b) Projection of $Li_2Bi_4Ti_3O_{12}$ cell along [110].
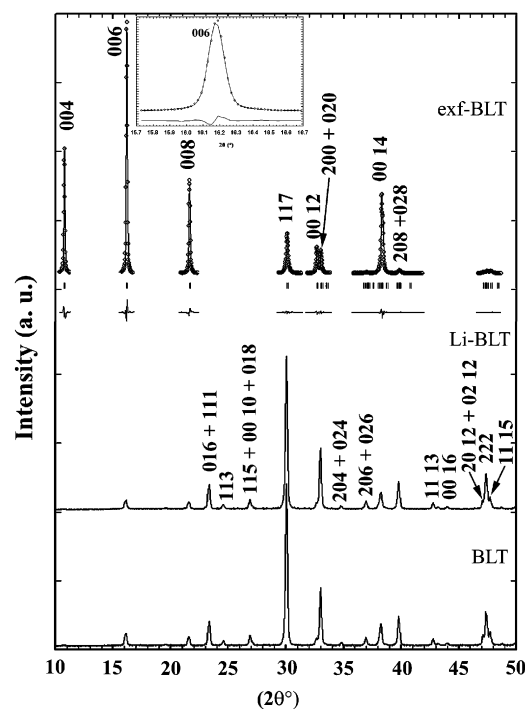

Fig. 2. X-ray diffraction patterns of pristine BLT, Li-BLT and exf-BLT. For exf-BLT, observed X-ray diffraction pattern (circles) and profile fitting (continuous line) on selected 2θ ranges are compared: the lower curve shows the value of the difference between the observed and calculated intensity at each step (refinement of the Gaussian profile shape parameter I_G). Tick marks indicate the positions of all possible Bragg reflections, constrained by cell parameters and generated from the space group $B2cb$. The inset is a zoom of the (006) reflection.

exfoliated BLT), the patterns exhibit rather poor statistic. This can be interpreted either by the poor crystallinity of our samples or by peak broadening due to microstructural

effects such as microstrains or small crystallite size. According to TEM observations (see below), we believe that the latter interpretation is more suitable, because the observed crystallites exhibit good crystallinity and all have a size less than 1 μm. Moreover, it is to be noticed that the BLT pristine material was thoroughly ground (manually) before lithiation. This is known to induce local strains in Aurivillius phases, as demonstrated by Muller et al. [35] on $SrBi_2Ta_2O_9$ (SBT) powders.

4.1.1. Comparison of the patterns of BLT and Li-BLT

The patterns of the BLT pristine material and LiBLT (Fig. 2) are nearly undistinguishable. This is consistent with the literature reports [19,36]. ICP results confirm the presence of lithium in the lithiated compound. All the cations are measured and the formula is determined to be $Li_{0.99}Bi_{3.25}La_{0.77}Ti_{3.00}O_{12}$. The lithium content is thus approximately half the one reported in literature for lithiated BTO [18,19,36]. These results confirm a topotactic intercalation including neither ordering of intercalated lithium, nor significative cell parameters changes. All peaks can be indexed in the orthorhombic symmetry (space group $B2cb$). This was checked by profile matching in which the position of all possible Bragg reflections are constrained by cell dimensions and space group. The poor statistic of the experimental patterns prevented the fitting of the data with whole-pattern-fitting-structure-refinement using the Rietveld method, where atomic coordinates are used to calculate structure factors and subsequently integrated intensities.

4.1.2. Comparison of the patterns of BLT and exfoliated BLT

A first pattern (not shown) collected on the exfoliated BLT sample, over the same angular range than the pristine material and with the same step counting time (50 s), has exhibited a significant preferred orientation along the c-axis together with a very poor signal/noise ratio. This is due to the weak amount of particles deposited on a Si substrate from a clear supernatant. For these reasons, a second pattern was collected on selected 2θ ranges, with a very long step counting time of 200 s. Fig. 2 shows the XRD pattern of the exfoliated BLT particles deposited on a (001)-Si substrate as described above. It shows two major changes as compared to that of the bulk powder: (i) a strong preferred orientation along the c-axis since only (00ℓ) reflections are observed and (ii) a significant broadening of the (00ℓ) peaks. The first point suggests that the exfoliated BLT is composed of platelets perpendicular to the c-axis. The second point may be interpreted in terms of size or microstrains effects.

4.2. Origin and quantification of diffraction line broadening

For the exfoliated material, we have tried to uncover the origin of the diffraction line broadening: size effect, independent of the order of reflection, or microstrain effects which are order-dependent. Considering the poor statistic of the exf-BLT pattern, the strongly marked preferred orientation and the truncated pattern, full pattern refinement was not possible. So, pattern matching including cell constants and profile parameters was conducted with the FULLPROF program. The microstructural effects within FULLPROF are treated using the Voigt approximation: both instrumental and sample intrinsic profiles are supposed to be described approximately by a convolution of Lorentzian and Gaussian components. The Thompson, Cox and Hastings (TCH) pseudo-Voigt profile function [37] is used to mimic the exact Voigt function. The advantage of this function is that it allows a correct convolution of the instrumental function with the intrinsic sample profile function, provided an input file containing the instrumental resolution function is used. As mentioned in Section 2, a sample of YIG was used for the instrumental profile function calibration. The integral breadth method is used to obtain volume averages of sizes and strains.

The FWHM (H) of the Gaussian (H_G) and Lorentzian (H_L) components of the profile has an angular dependence given by

$$H_G^2 = U \times \tan^2\theta + \frac{I_G}{\cos^2\theta},$$

$$H_L = X \times \tan\theta + \frac{Y}{\cos\theta}.$$

The four profile parameters in the above formulae have a meaning in terms of strain (U, X) or size (I_G, Y). Indeed, it is well known from Scherrer formula ($\beta = \lambda/(\Delta \times \cos\theta)$, where β is the integral breadth of the profile, λ the wavelength of the X-ray beam and Δ the apparent crystallite size) that size broadening has an angular dependence on $1/\cos\theta$. Microstrains also broaden the diffraction profile with an angular dependence in $\tan\theta$ according to the formula: $\beta = (\Delta d/d) \times \tan\theta$, where $\Delta d/d$ represents the dispersion in reticular spacing. The size contribution to integral breadth β_{size} is obtained from $H_{G(size)}$ and $H_{L(size)}$ whereas the strain contribution to β_{strain} is extracted from $H_{G(strain)}$ and $H_{L(strain)}$ [35]. Finally, the apparent size (in Å) and strain (in %) are calculated using the formulae:

$$\text{App. size} = \frac{1}{\beta_{size}},$$

$$\text{App. strain} = 0.5 \times \beta_{strain} \times d_{hkl}.$$

The four profile parameters described above, namely, I_G, Y, U and X were successively and independently refined in order to determine which parameters gave the better agreement between calculated and observed patterns [35].

In addition, a careful examination of the bottom of the (00ℓ) peak profile has revealed a peculiar shape, which might be described from a weak and broad contribution superimposed with a narrow and large contribution. This feature could be an indication of the existence of a bimodal

Table 1
Details of the profile fitting on exf-BLT XRD data

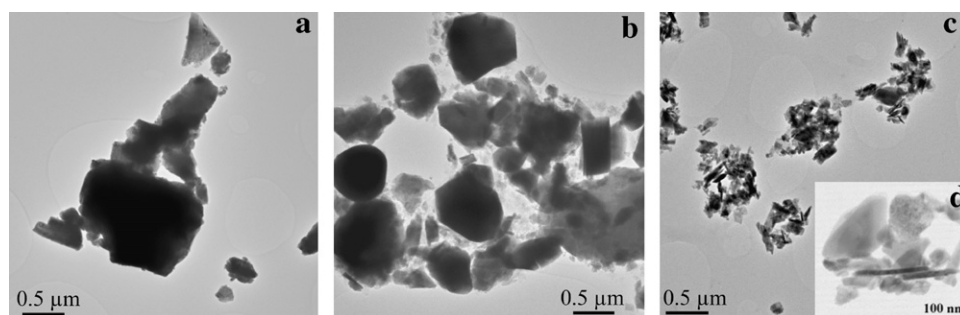| Refined parameter	Average max strain (‰)		Average apparent size (nm)		R_p (%)	R_{wp} (%)	χ^2
	Population 1	Population 2	Population 1	Population 2			
Two populations of crystallites							
U	16.868 (1)	52.82 (1)	–	–	5.3	9.5	11.8
X	16.781 (8)	23.35 (2)	–	–	9.3	12.4	21.5
I_G	–	–	110.17 (8)	25.11 (1)	5.4	7.1	6.6
Y	–	–	149.66 (2)	37.04 (1)	8.2	10.6	15.7
Only one population of crystallites							
I_G		–	92.84 (4)		11.5	16.0	33.1

Fig. 3. General views of the different powders: (a) initial BLT powder, (b) lithiated BLT powder, (c) exfoliated BLT powder, (d) zoom on the exfoliated BLT powder.

distribution of crystallite sizes in the sample. For this reason, the refinements were conducted including either one or two "phases" corresponding, respectively, to a single one or two population(s) of crystallite sizes.

Whatever the refined parameter, the introduction of two populations rather than a single one improves the peak fitting at the bottom and subsequently the pattern reliability factors. The results are given in Table 1. The better fit was obtained when the parameter I_G was refined, this feature confirming that the (00ℓ) peak broadening is mainly due to a size effect. Besides, the existence of a bimodal size distribution is demonstrated, since reliability factors are drastically improved when introducing a second population of small crystallites. The refinement gives an average apparent size of 110 ± 16 nm along the *c*-axis direction for the first population (largest crystallites) and 25 ± 3 nm for the second population (small crystallites). The fitted pattern obtained in refining I_G parameter is depicted in Fig. 2.

4.3. Electron microscopy results

Electron microscopy was performed to obtain overall views of the powders as well as local structural information from high-resolution imaging. On the exfoliated powder, the attention has been turned towards the smallest particles. In the following, the Fourier transforms of the images are systematically shown in inset in figures in order to establish the orientation of the particles. HREM image simulations are obtained from a cell of BTO with a partial

substitution of Bi^{3+} by La^{3+} in the perovskite site [34]. Besides, image simulations enable determining which cation planes are linked to the main patterns in the experimental image: these identifications may be useful when studying the exfoliated BLT powder. Results were obtained on BLT, on LiBLT and on exfoliated BLT. Fig. 3a–c shows typical general views of each powder obtained at the same scale. The stoichiometry of each powder was verified on a great number of particles by EDS analyses. The results are very homogeneous and give a ratio of 0.76 ± 0.03 for the lanthanum substitution ratio. This composition is the same in all powders.

4.3.1. Results on pristine BLT powder

Fig. 3a shows a typical general view of the BLT pristine powder: one can see that the size of the particles is not homogeneous but most of them are submicronic. Some of the grains have elongated shapes with sizes ranging from 50 to 800 nm; others are isotropic with an average size around 160 nm. Many aggregates can be seen.

The indexation of electron diffraction patterns obtained on grains of this powder (which are not presented here) respect the selection rules of the *B2cb* space group. No extra reflections suggesting an ordered substitution of cation were observed. In the same way, we can state that there is no structural distortion.

The HREM images obtained along [100] (Fig. 4a) and [110] (Figs. 5a and 6a) directions show the piling up of fringes perpendicular to the *c* crystallographic axis. One can see that, despite careful manual grinding, the initial
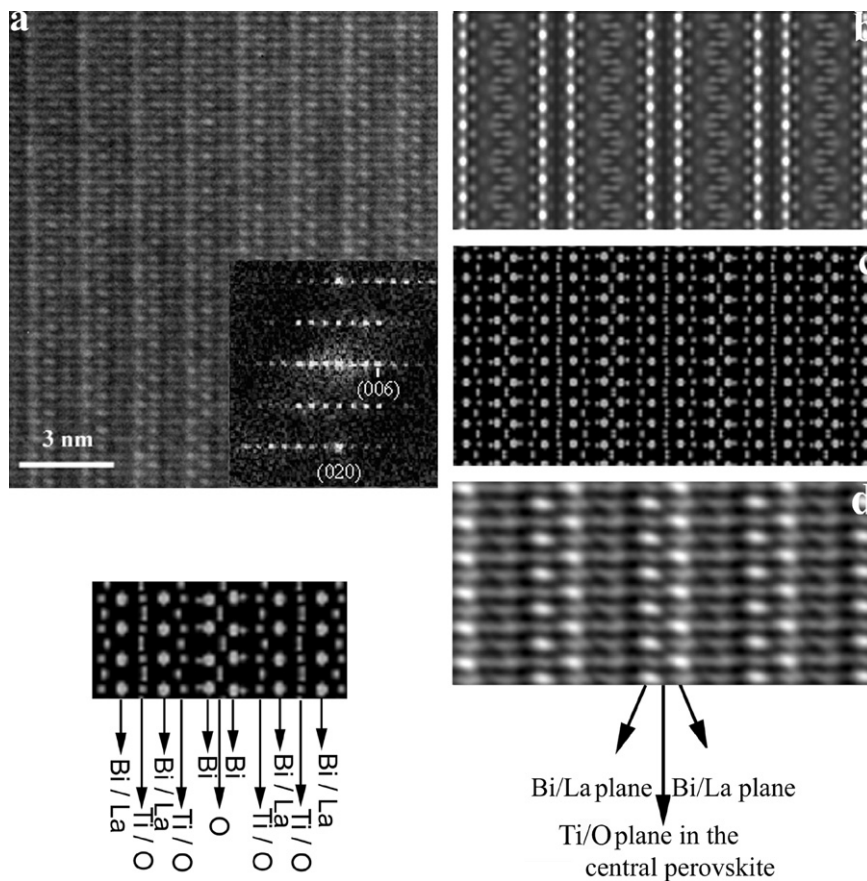
Fig. 4. (a) HREM image of a grain of initial powder along [100] (inset Fourier transform); (b) simulated image along [100], defocus $= -40$ nm and thickness $= 9$ nm; (c) model of the $Bi_{3.25}La_{0.75}Ti_3O_{12}$ cell projected along [100]; (d) Bragg filtered image.
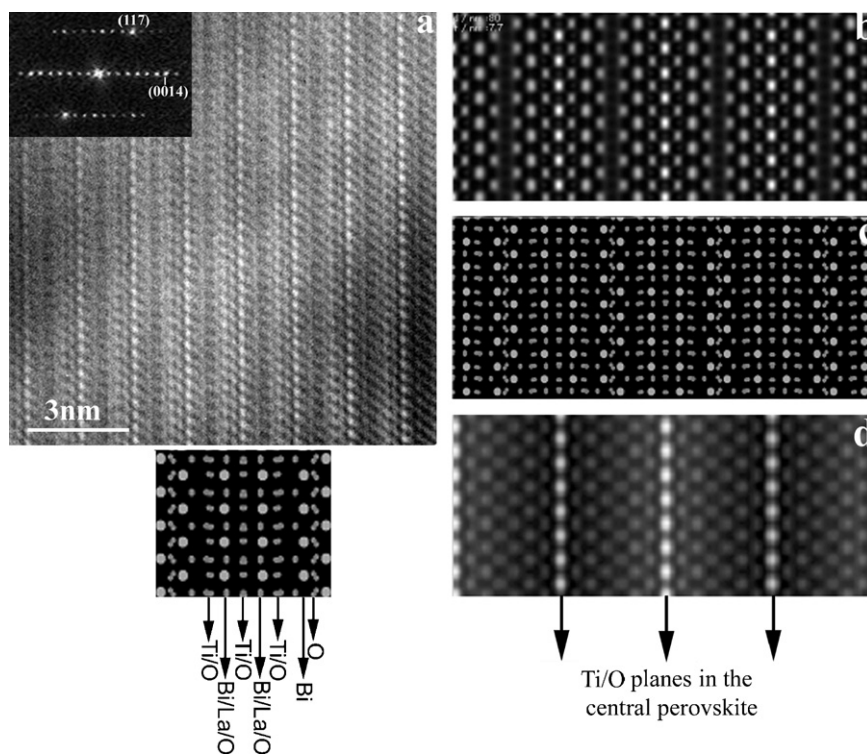

Fig. 5. (a) [110] HREM image of a grain of the initial BLT powder (inset Fourier transform); (b) simulated image along [110], defocus $= -80$ nm and thickness $= 7.7$ nm; (c) model of the $Bi_{3.25}La_{0.75}Ti_3O_{12}$ cell projected along [110]; (d) Bragg filtered image.
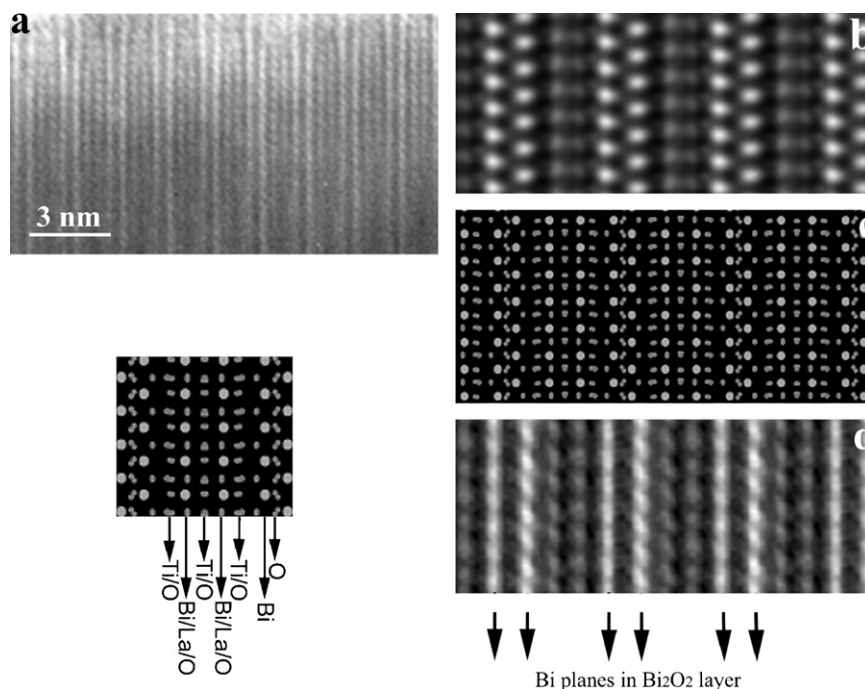
Fig. 6. (a) [110] HREM image of a grain of the initial BLT powder; (b) simulated image along [110], defocus $= -60$ nm and thickness $= 7.7$ nm; (c) model of the $Bi_{3.25}La_{0.75}Ti_3O_{12}$ cell projected along [110]; (d) Bragg filtered image.

BLT powder shows a nearly perfect structure. From a series of HREM image simulations calculated at different values of defocus and for different thicknesses of the sample, we notice that the simulation image (Fig. 4b), which reproduces the main aspects of the experimental Bragg filtered image (Fig. 4d), corresponds to a sample thickness around 9 nm and a defocus value of -40 nm. Comparison with the model (Fig. 4c) and the experimental Bragg filtered image (Fig. 4d) shows that the dark line bordered by two white fringes in the image corresponds to the Ti plane in the central perovskite of the structure, the one which is nearly not distorted. Measurements, on the experimental image, show that only 12 cations planes are visible, the intermediate Bi_2O_2 layer being not well resolved. The [110] image (Fig. 5a) exhibits a different pattern with one fringe brighter than the others; comparison with simulated image (Fig. 5b) shows now that this bright fringe corresponds to the Ti–O plane in the central perovskite. In this case, all cation planes are imaged. Finally, the other [110] image (Fig. 6a) shows a pattern similar to the one in Fig. 4a; but simulations indicate that the double white fringe is now linked to the intermediate layer while, in the pseudo-perovskites blocks, only the Bi planes are imaged.

The study of the different series of HREM images as well as electron diffraction patterns enable concluding that no cation substitution ordering and no structural distortions appear in the BLT pristine powder.

4.3.2. Results on lithiated BLT powder

On Li-BLT powder, TEM images are difficult to obtain as, when submitted to electrons bombardment, Li^+ cations tend to leave the sample, causing bubbles (see Fig. 7b) but also cracks at the edge of the grains (see for instance Fig. 7b–d). Fig. 3b shows a general view of the sample: the grains are similar in morphology and size to the initial BLT powder. However, when zooming (Fig. 7a and b) or looking at HREM images (Fig. 7c and d), one can see that the particles are perturbed. The structure of Li-BLT is nearly the same as BLT and Li^+ cations are too light to produce detectable effects in HREM image so that the same patterns appear. The only difference is the apparition of cracks under electron beam, either in small particles (Fig. 7b) or in large ones (Fig. 7c and d). This phenomenon has never been observed in the pristine material. Cracks are always perpendicular to the c-axis and the particles often present staircase boundaries.

4.3.3. Results on exfoliated BLT powder

Fig. 3c shows a typical general view of exf-BLT powder obtained from the clear supernatant. One can see clearly that the average size is much smaller than before exfoliation (Fig. 3a and b). The particles are sticks or platelet-shaped and appear either edge-on or lying flat (Fig. 3d). Obviously, during the TEM study, we have focused on the small particles but no statistical treatment of the nanosheet thickness was done. All the observed platelets have their plane normal to the c-axis. In the following, a peculiar attention has been turned towards the edge-on particles since they show the stacking along the c-axis. They also give a straightforward measurement of the platelets thickness. Fig. 8 shows the smallest platelet observed with a thickness of 3.3 nm corresponding to one cell parameter along the c-axis.
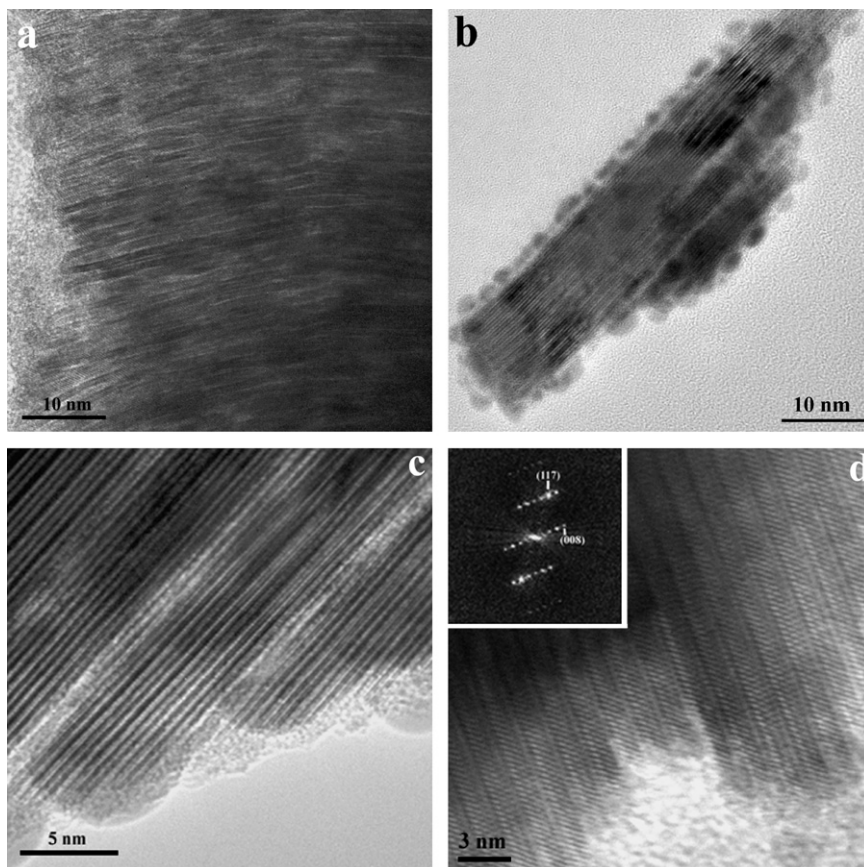
Fig. 7. (a) Image of a perturbed Li-BLT grain; (b) image of a damaged Li-BLT grain; (c) zoom on a Li-BLT grain; (d) HREM image of a Li-BLT grain viewed along the [110] direction.
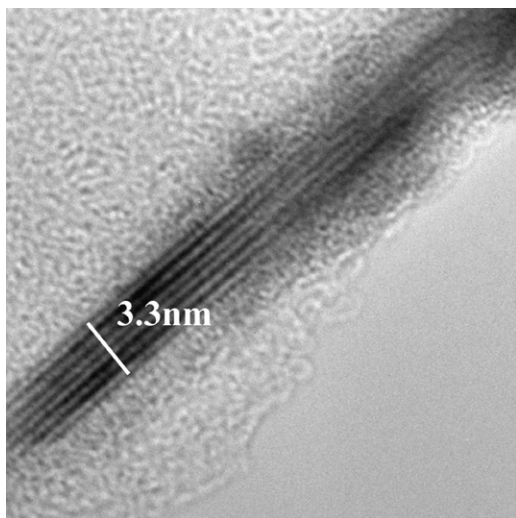

Fig. 8. Image of a nanosheet in the exf-BLT powder.

Figs. 9 and 10 show some examples of HREM images of edge-on platelets. The first one (Fig. 9a), [110] oriented, exhibits five half c periods, corresponding to a platelet thickness around 8 nm. The best agreement between simulated and experimental images is obtained at a defocus of -70 nm (very close to Scherzer defocus) for which the

Bi_2O_2 layers are imaged as two bright lines of white dots. One can see that the edge of the platelet corresponds to the end of the perovskites group: indeed, on all images where the edge can be observed without blurring from Fresnel fringes, the same phenomenon is observed. This proves that exfoliation occurs in the Bi_2O_2 layer, which is destroyed in most cases. However, sometimes, a fragment of Bi_2O_2 layer remains, shown by an arrow in the image (Fig. 9a).

Fig. 10a exhibits another example where the platelet thickness is around 12 nm. In this case, the white fringe corresponds to the central perovskite. The 14 cations planes are imaged on a profile drawn along one period parallel to the c-axis. When compared to a profile drawn on simulated image, no difference is seen: the distances between the fringes are identical and no defect is observed, even at the Bi_2O_2 layers where there should have been Li^+ cations before exfoliation.

Finally, a larger density of defects was detected in few grains with much larger sizes. As shown in Fig. 11, the general appearance is similar to the Li-BLT (Fig. 7) with cracks near the grain edge (shown by arrows). It looks as if the exfoliation could not be carried out in the whole grain. The areas 1 and 3 correspond to perfect crystals (as shown by their Fourier transforms) whereas, in area 2, which is over the crystal and the separations, the Fourier transform
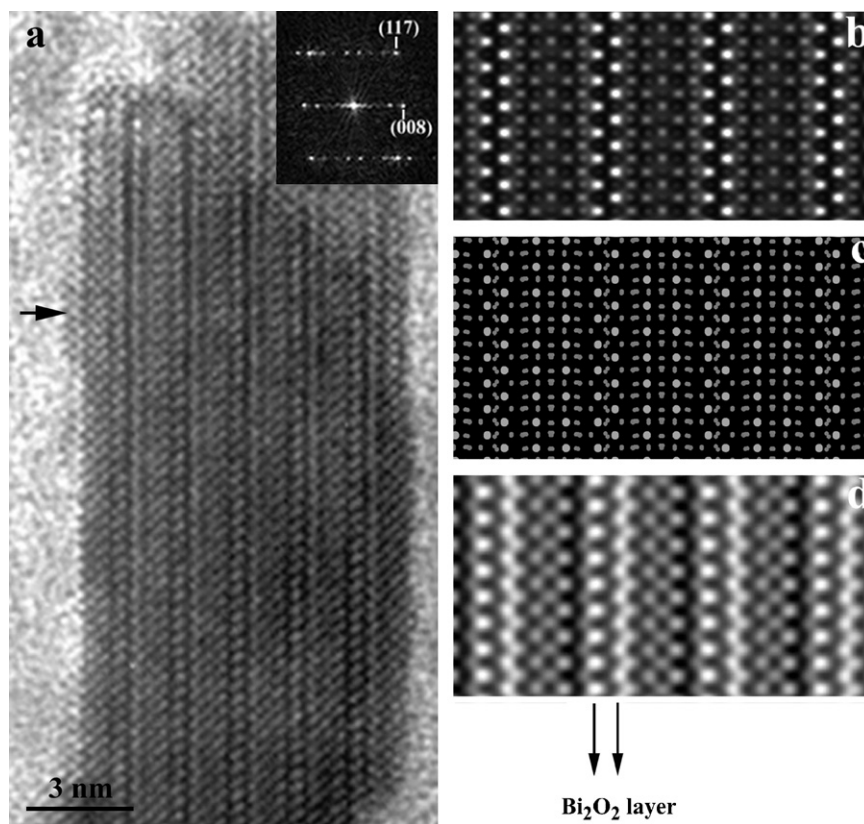
Fig. 9. (a) [110] HREM image of a grain of the exf-BLT powder (inset Fourier Transform); (b) simulated image along [110], defocus $= -70$ nm and thickness $= 5.4$ nm; (c) model of the $Bi_{3.25}La_{0.75}Ti_3O_{12}$ cell projected along [110]; (d) Bragg filtered image.
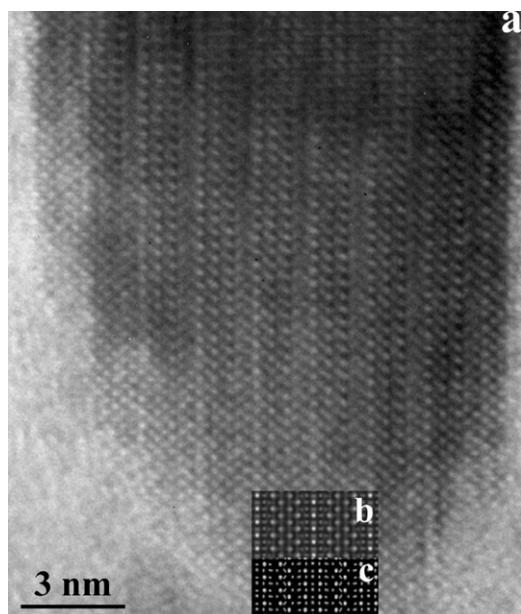

Fig. 10. (a) [110] HREM image of a grain of the exf-BLT powder; (b) simulated image along [110], defocus $= -90$ nm and thickness $= 7.7$ nm; (c) model of the $Bi_{3.25}La_{0.75}Ti_3O_{12}$ cell projected along [110].

Fig. 11. Medium-resolution image of a grain of the exf-BLT powder with steps (insets: Fourier transforms of three zones).

presents diffuse scattering between the diffraction spots. This feature is characteristic of a strongly perturbed stacking of the $(0\,0\,\ell)$ planes.
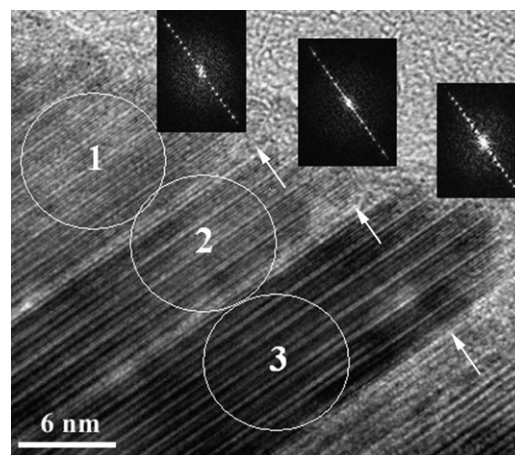
5. Discussion

Three main conclusions can be drawn from the whole results of this work. First, lithiation and subsequent exfoliation of BLT can be achieved by the same soft chemical redox process than the one used by Kim et al. [18] for BTO. Secondly, the location of Li^+ cations in the $(Bi_2O_2)^{2+}$ layers, as claimed by Choy et al. [19] according to neutron diffraction experiments, is confirmed. Indeed,

HREM and simulations images allow us to state that the surfaces of the exfoliated platelets are invariably located at the end of the perovskites group in the structure of BLT. Moreover, our images also show that these Li-filled $(Bi_2O_2)^{2+}$ layers are destroyed during the exfoliation process. Third and last conclusion, according to ICP analysis, the formula $LiBi_{3.25}La_{0.75}Ti_3O_{12}$ shows that the amount of inserted lithium in BLT is only half the one than in BTO.

Let us start the discussion with the two first points. The ability of the Aurivillius phases to undergo intercalation is not self-evident: contrary to the other perovskite layered compounds (D–J and R–P phases) or other layered compounds such as graphite, clays or metal dichalcogenides, which are all characterised by strong intralayer bonding and weaker interlayer interactions, the Aurivillius phases do not have a Van der Waals gap, either empty, partially or completely filled by ions, but a strong iono-covalent bonding in $(Bi_2O_2)^{2+}$ layers. To understand why this intercalation takes place so easily, the most suitable way to describe Aurivillius compounds is probably as ABO_3 perovskites with ordered vacancies on B-site; indeed, the skeleton of oxygen ions in these compounds is a slightly distorted perovskite oxygen lattice. The A-sites are all occupied while, for the general formula $Bi_2O_2A_{m-1}B_mO_{3(m+1)}$, one over $m+1$ B-site is vacant: the formula should be written as $m+1$ perovskites $(Bi_2A_{m-1})(B_mV)O_{3(m+1)}$ where V is a vacancy over the B-site. One has to take a larger cell including at least $m+1$ perovskite cells. Around the vacancy, strong distortions occur as can be seen in Fig. 1a and b: in the case of BTO ($m=3$, $A=$ Bi) one Ti plane over four is missing, while all the four Bi planes are occupied. Around the Ti vacancy, the two Bi planes are disturbed: along the c-axis, they are nearer one to the other than in a normal perovskite. In the a–b plane, the bismuth ions are translated giving rise to a difference of $a/2$ between their positions. This explains why the following sequence of four perovskites is translated, as said in Section 3. The existence of the vacancies produces a strong disorganisation at the level of this perovskite group but the oxygen plane, where the Ti vacancies are, is only weakly altered. It is very understandable that when intercalating another cation, Li^+ in this work, it should go in the perturbed perovskite, that is to say, in the so-called $(Bi_2O_2)^{2+}$ layers where vacancies exist. In these layers, Bi^{3+} cations are eight-fold coordinated, they will be noticed Bi(8) hereafter. It should be reminded here that these Bi^{3+} sites are free from lanthanum in BLT as in BTO. The two compounds have then the same number of Bi(8) site per formula.

This leads to comment the amount of inserted lithium in BLT and BTO. From ICP and atomic absorption spectroscopy methods, Choy et al. found a formula $Li_{2.1}Bi_4Ti_3O_{12}$ for the lithiated BTO. With a Li:Bi(8) molar ratio equal to 1:1, the lithium insertion appears to be "complete" in BTO, that is to say with Li^+ cations inserted in each $(Bi_2O_2)^{2+}$ layers on average. This result is confirmed by Rietveld

analysis conducted on neutron data, which allowed them to propose the structure shown in Fig. 1. As a consequence, the exfoliation should lead to single sheets with a thickness of 1.6 nm (half a c-cell parameter). However, this is not the case: the nanoplatelets have an average thickness of 4.8 nm (corresponding to three half c-cell parameters) [18]. In our work, with a Li:Bi(8) molar ratio equal to 1:2, only one over two $(Bi_2O_2)^{2+}$ layers should be occupied on average. However, the large range of platelet thicknesses obtained in the exfoliated sample shows that exfoliation has not occurred in all presumably occupied layers.

It could be tempting to consider that this large range of platelet thicknesses results from the restacking of thinner particles, in the absence of surfactant usually used to stabilise nanosheets in aqueous colloidal suspensions. Notably, the particle shown in Fig. 11 could at first sight be interpreted this way, but this hypothesis can be dismissed. Indeed, if spontaneous restacking of single nanosheets had happened, it should have led to strongly perturbed stacking in the resulting thicker nanosheets, owing to the destruction of the $(Bi_2O_2)^{2+}$ layers during exfoliation. Such a strongly perturbed nanosheet is presented in Fig. 12, but this case is seldom seen.

Therefore, there ought to be another origin to the discrepancy between the observed thicknesses and the expected ones. It may result from two concomitant phenomena: in some layers, Li^+ cations could have not diffused sufficiently right to the centre of the grain to promote exfoliation, while other $(Bi_2O_2)^{2+}$ layers could accommodate more than one lithium cation per Bi(8) site. This second point seems to be confirmed by the formula $Li_{2.38}Bi_4Ti_3O_{12}$ found by Kumar et al. [36] for their lithiated BTO compound (ICP results). This would result in lithium local surconcentration rather than an uniform distribution in all $(Bi_2O_2)^{2+}$ layers. This is supported by the apparition of rather scarce and irregularly distributed cracks at the edges of the grain in the lithiated compound (see Fig. 7c and d) under the electron beam. A local
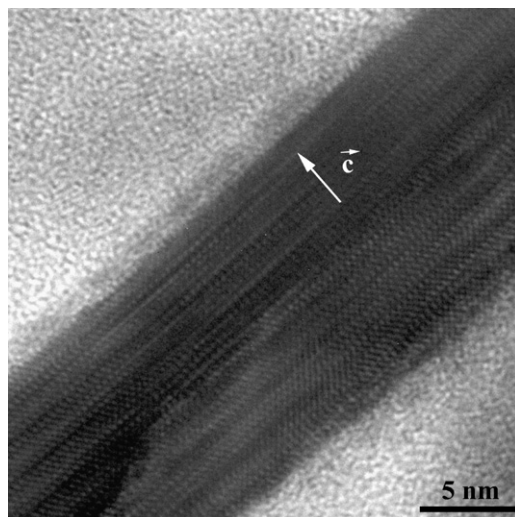

Fig. 12. HREM image of two [110] nanosheets of BLT restacked.

surconcentration of lithium could promote the separation of the sheets during "exfoliation" in water.

It remains to understand why, for BLT, this amount of lithium is only half the one as in BTO. Several hypotheses can be advanced. First, intercalation reactions generally seem to be initiated at defects on the host surface, and therefore variations in reactivity often arise from one batch to another due to microcrystalline or particle size differences of the initial solid [12]. This is why we have so carefully characterised our pristine materials. All our syntheses on BLT lead to the same results, i.e. to regular defects-free grains. This probably does not promote lithium intercalation. It is possible that the unalike behaviours of BTO and BLT towards lithium intercalation simply result from microstructural differences in the pristine materials. A second possibility is that it is more difficult, for lithium cations, to intercalate in BLT than in BTO. From a structural viewpoint, it has been proposed [36] that the intercalation of lithium in BTO relaxes the local strains existing in the $(Bi_2O_2)^{2+}$ layers. The substitution of La^{3+} for Bi^{3+} ($x \leqslant 1$) in BTO is known to decrease the mismatch between the $(Bi_2O_2)^{2+}$ layers and the perovskite blocks and subsequently relieves the strains [33,34]. One might thus hypothesise that lithium intercalation is less favourable in BLT than in BTO since strains have already been relaxed by lanthanum substitution.

6. Conclusion

Particles of the Aurivillius phase, La-substituted BTO, were obtained through a chemical lithiation/exfoliation process. The substitution ratio of lanthanum is constant in all powders and is equal to 0.76 ± 0.03. The studies, performed by XRD and TEM, show clearly that the average particle size has decreased in the exfoliated BLT powder in comparison with the pristine BLT powder. The pattern collected on the exfoliated BLT sample presents a strong preferential orientation: only the (00ℓ) reflections are observed. Exfoliation leads to [001] BLT particles which are distributed in two populations: the smallest one corresponds to nanosheets, with an average thickness around 25 nm. All the observed exfoliated particles have a thickness corresponding to a multiple of $c/2$ and inferior or equal to 25 nm. The smallest thickness observed is 3.3 nm, corresponding to one BLT cell parameter along the c-axis. From the high-resolution images, we can say that most of the particles are well crystallised and present few defects. The electron diffraction patterns and the HREM images, obtained on the exfoliated particles, are in agreement with the selection rules of the $B2cb$ space group like those obtained on the grains of the initial powder. Thus, it is shown that the nanosheets have the same crystallographic stacking as the BLT parent phase. The HREM and the corresponding simulation images show that the delamination process occurs at the level of the $(Bi_2O_2)^{2+}$ intermediate layer and is destructive for this layer. In our case, the exfoliation does not lead to single perovskite sheets. Surprisingly, it seems that the partial substitution of bismuth with lanthanum lowers the amount of intercalated Li^+ cations comparatively to what was observed in Li-BTO. Li^+ intercalation appears to be quite heterogeneous in our case. However, this could also be due to the defect free morphology of the pristine material.

References

[1] M. Dion, M. Ganne, M. Tournoux, Mater. Res. Bull. 16 (1981) 1429.
[2] M. Dion, M. Ganne, M. Tournoux, J. Revez, Rev. Chim. Miner. 21 (1984) 92.
[3] S.N. Ruddlesden, P. Popper, Acta Crystallogr. 10 (1957) 538.
[4] S.N. Ruddlesden, P. Popper, Acta Crystallogr. 11 (1958) 54.
[5] J. Gopalakrishnan, V. Bhat, Inorg. Chem. 26 (1987) 4301.
[6] B. Aurivillius, Ark. Kemi 1 (1949) 463.
[7] B. Aurivillius, Ark. Kemi 1 (1949) 499.
[8] J. Van Landuyt, G. Remaut, S. Amelinckx, Mater. Res. Bull. 4 (1969) 329.
[9] E. Sawaguchi, L.E. Cross, Mater. Res. Bull. 5 (1970) 147.
[10] R.E. Newnham, R.W. Wolfe, J.F. Dorrian, Mater. Res. Bull. 6 (1971) 1029.
[11] R.E. Schaak, T.E. Mallouk, Chem. Mater. 14 (2002) 1455.
[12] D. O'Hare (chapter 4), R.W. McCabe (chapter 6), in: Inorganic Materials, D.W. Bruce, D. O'Hare (Eds.), Wiley, Chichester, 1997.
[13] J.H. Choy, J. Phys. Chem. Solids 65 (2004) 373.
[14] M. Fang, H.N. Kim, G.B. Saupe, T. Miwa, A. Fujishima, T.E. Mallouk, Chem. Mater. 11 (1999) 1526.
[15] R.E. Schaak, T.E. Mallouk, Chem. Mater. 12 (2000) 2513.
[16] R.E. Schaak, T.E. Mallouk, Chem. Mater. 12 (2000) 3427.
[17] S.G. Denis, J.C. Simon, Chem. Commun. (2001) 2356.
[18] J.Y. Kim, I. Chung, J.H. Choy, Chem. Mater. 13 (2001) 2759.
[19] J.H. Choy, J.Y. Kim, I. Chung, J. Phys. Chem. B 105 (2001) 7908.
[20] P.C. Joshi, S.B. Krupanidhi, Appl. Phys. Lett. 62 (1993) 1928.
[21] B.H. Park, B.S. Kang, S.D. Bu, T.W. Noh, J. Lee, W. Jo, Nature 401 (1999) 682.
[22] Y.W. So, B.S. Kang, S.A. Seo, D.J. Kim, T.W. Noh, J.G. Yoon, Ferroelectrics 271 (2002) 347.
[23] A. Kingon, Nature 401 (1999) 658.
[24] M.W. Chu, M. Ganne, M.T. Caldes, L. Brohan, J. Appl. Phys. 91 (2002) 3178.
[25] M.W. Chu, M. Ganne, P.Y. Tessier, D. Eon, M.T. Caldes, L. Brohan, Mater. Sci. Semicond. Proc. 5 (2003) 179.
[26] J. Rodriguez-Carvajal, Physica B 192 (1993) 55.
[27] P.A. Stadelmann, Ultramicroscopy 21 (1987) 131.
[28] A.D. Rae, J.G. Thompson, R.L. Withers, A.C. Willis, Acta Crystallogr. B 46 (1990) 474.
[29] C.H. Hervoches, P. Lightfoot, Chem. Mater. 11 (1999) 3359.
[30] Y. Shimakawa, Y. Kubo, Y. Tauchi, H. Asano, T. Kamiyama, F. Izumi, Z. Hiroi, Appl. Phys. Lett. 79 (2001) 2791.
[31] A.Z. Simoes, C. Quinelato, A. Ries, B.D. Stojanovic, E. Longo, J.A. Varela, Mater. Chem. Phys. 98 (2006) 481.
[32] M.W. Chu, M.T. Caldes, L. Brohan, M. Ganne, A.M. Marie, O. Joubert, Y. Piffard, Chem. Mater. 16 (2004) 31.
[33] C.H. Hervoches, P. Lightfoot, J. Solid State Chem. 153 (2000) 66.
[34] M.W. Chu, Thesis, University of Nantes, 2002.
[35] Ch. Muller, F. Jacob, Y. Gagou, E. Elkaïm, J. Appl. Crystallogr. 36 (2003) 880.
[36] S. Kumar, M. Panneerselvam, P. Vinatier, K.J. Rao, Ferroelectrics 306 (2004) 165.
[37] P. Thompson, D.E. Cox, J.B. Hastings, J. Appl. Crystallogr. 20 (1987) 79.